Provided for non-commercial research and education use.
Not for reproduction, distribution or commercial use.

Volume 314, Number 1, October 1, 2007
ISSN 0021-9797
ELSEVIER

JOURNAL OF Colloid and Interface Science

EDITOR-IN-CHIEF
Darsh T. Wasan
Illinois Institute of Technology, Chicago

CO-EDITORS

Julian Eastoe
University of Bristol, United Kingdom

Arthur T. Hubbard
Santa Barbara Science Project, California

Manuel Arturo López-Quintela
University of Santiago de Compostela, Spain

Gao Qing Lu
University of Queensland, Australia

Martin Malmsten
Uppsala University, Sweden

ADVISORY BOARD

Masahiko Abe
Chiba, Japan
Pierre M. Adler
Paris, France
Jayesh Bellare
Mumbai, India
Marcel Böhmer
Eindhoven, Netherlands
Peter Bräuer
Leipzig, Germany
Richard Finke
Colorado, USA
Peter Griffiths
Cardiff, UK
Andrew Howe
Cambridge, UK
Marek Kosmulski
Lublin, Poland
Dongqing Li
Tennessee, USA
Louis Liz Marzan
Vigo, Spain
Stefano A. Mezzasalma
Trieste, Italy
Jerzy Mielczarski
Vandoeuver-les-Nancy, France
Catherine J. Murphy
South Carolina, USA
Tommy Nylander
Lund, Sweden
Clive A. Prestidge
Mawson Lakes, Australia
John Ralston
Mawson Lakes, Australia
Eli Ruckenstein
New York, USA
Lynn M. Walker
Pennsylvania, USA
Gregory G. Warr
Sydney, Australia
Fernando Wypych
Curitiba, Brazil
Joseph Zazadzinski
California, USA
Thomas Zemb
Gif-sur-Yvette, France
Dongyuan Zhao
Shanghai, China

Victor K. La Mer, Editor 1946–1965
Albert C. Zettlemoyer, Co-Editor 1965–1987
Milton Kerker, Co-Editor 1965–1987, Editor 1987–1992
Josip P. Kratohvil, Co-Editor 1987–2004
Hironobu Kunieda, Co-Editor 2004–2005

This article was published in an Elsevier journal. The attached copy is furnished to the author for non-commercial research and education use, including for instruction at the author's institution, sharing with colleagues and providing to institution administration.

Other uses, including reproduction and distribution, or selling or licensing copies, or posting to personal, institutional or third party websites are prohibited.

In most cases authors are permitted to post their version of the article (e.g. in Word or Tex form) to their personal website or institutional repository. Authors requiring further information regarding Elsevier's archiving and manuscript policies are encouraged to visit:

http://www.elsevier.com/copyright

Available online at www.sciencedirect.com
ScienceDirect
Journal of Colloid and Interface Science 314 (2007) 264–273
Journal of Colloid and Interface Science
www.elsevier.com/locate/jcis

Electroosmosis in homogeneously charged micro- and nanoscale random porous media

Moran Wang [a,b,*], Shiyi Chen [b,c]

[a] *Department of Biological and Agricultural Engineering, University of California, Davis, CA 95616, USA*
[b] *Department of Mechanical Engineering, The Johns Hopkins University, Baltimore, MD 21218, USA*
[c] *College of Engineering and LTCS, Peking University, Beijing, China*

Received 19 April 2007; accepted 16 May 2007

Abstract

Electroosmosis in homogeneously charged micro- and nanoscale random porous media has been numerically investigated using mesoscopic simulation methods which involve a random generation-growth method for reproducing three-dimensional random microstructures of porous media and a high-efficiency lattice Poisson–Boltzmann algorithm for solving the strongly nonlinear governing equations of electroosmosis in three-dimensional porous media. The numerical modeling and predictions of EOF in micro- and nanoscale random porous media indicate that the electroosmotic permeability increases monotonically with the porosity of porous media and the increasing rate rises with the porosity as well; the electroosmotic permeability increases with the average solid particle size for a given porosity and with the bulk ionic concentration also; the proportionally linear relationship between the electroosmotic permeability and the zeta potential on solid surfaces breaks down for high zeta potentials. The present predictions agree well with the available experimental data while some results deviate from the predictions based on the macroscopic theories.

Keywords: Random porous media; Electroosmosis; Lattice Poisson–Boltzmann method; Mesoscopic simulation

1. Introduction

Electroosmotic flows (EOFs) in porous media have been studied for nearly 200 years due to their important applications in soil, petroleum, and chemical engineering [1–6] since the electrokinetic effects were first observed by Reuss in 1809 in an experimental investigation on porous clay [7]. In the past few decades, there is considerable and reawakening interest in the EOF in porous media because of the conspicuous applications in biological–chemical–medical analysis [8–11] and new techniques in energy and geophysical engineering [12–15], especially in micro- and nanoscales [16–18]. Recently, charged porous structures have been employed in some devices to control and improve the fluid behavior as expected. For example, microparticles which are packed in microchannels have been used to improve the performances of electroosmotic micropumps with a lower flow rate and a higher pumping pressure [19–24].

Although EOFs in porous media have been studied much theoretically, it is still a big challenge to predict the multiphysical transport behaviors in porous media accurately and efficiently due to its complicacies [25–35]. Levine and Neale [25] developed a "cell model" to predict the electroosmosis in multiparticle systems where the porous medium was considered as a random assemblage consisting of identical unit "cells," each of which contained a particle surrounded by a fluid envelope [26]. Although good results were obtained for disperse systems [27,28], the cell model did not deal well with dense porous media cases (i.e., at low porosities) because the model ignored the contacts and connections between particles [29]. By improving the "capillary tube model" [30], Mehta and Morse [31] schematized a microporous membrane by an array of charged uniform spheres. Jin and Sharma [32] extended the capillary model to a two-dimensional square lattice network model, which was more appropriate in simulating inho-

---

[*] Corresponding author.
E-mail address: mmwang@ucdavis.edu (M. Wang).

0021-9797/$ – see front matter © 2007 Elsevier Inc. All rights reserved.
doi:10.1016/j.jcis.2007.05.043

mogeneous porous media. Grimes et al. [33] developed the cubic lattice network of interconnected cylindrical pores model and simulated the intraparticle electroosmotic volumetric flow rate in the three-dimensional pore network of interconnected cylindrical pores. All these theoretical models are creative and contributive; however, there are still two defects so far when they are used for predictions of EOFs in micro- and nanoscale porous media. First, most of the models are based on vanishingly thin electric double layers (EDL) [19–22,25–35] so that they are not suitable for dense micro- and nanoscale porous media where the small pore space may be in a same order of the EDL thickness. Second, the theoretical models can hardly provide flow structure details, which are necessary for a deep understanding of the transport mechanism of electroosmosis in micro- and nanoscale porous media.

Owing to the rapid development of computer and computational techniques various numerical methods have been developed in the past decade for modeling and predicting multiphysical transport in porous media. A full numerical tool set for analyzing EOF in porous media needs two steps: a digital description of porous microstructure details and a set of partial differential equation (PDE) solvers for solving governing equations of the multiphysical transport phenomena. For EOF in microscale charged random porous media, both presented big challenges until now.

First, the microstructures of porous media are very complicated. The shapes and positions of pores/particles are random so that there could never be two natural porous media that are exactly the same. People can only reproduce microstructures of porous media based on the known macroscopic statistical information. Tacher et al. [36] and Pilotti [37] developed methods to generate granular porous media using spheres or ellipses with random sizes and locations; however, they could hardly deal with the intergrain connections. To make the reproduced structure more natural, the reconstruction process [38–42] has been widely used in generations of multiphase porous structures based on the digital microtomographic information and statistical correlation functions [41,42]. Similar algorithms have been found in soil research, named Markov chain Monte Carlo methods, which also created two-dimensional structures with satisfactory agreement with various scanned real soil structure images [43,44]. Borrowing the spirit of cluster growing theory [45,46], Wang et al. have recently developed a random generation-growth method to generate random microstructures of various multiphase microporous media including granular porous media [47,48] and fibrous porous media [49]. The generated structures have been used to predict effective thermal properties of porous materials and good agreements have been obtained with the existing experimental data [47,48].

Second, numerically solving the governing equations of EOF in porous structures is still quite challenging for the present computational methods [50–66]. The coupled electrostatic, hydrodynamic, and mass transport problems subjected to complex geometrical boundary conditions represented by the solid–liquid interface in random porous media require huge or even unacceptable computational resources. The difficulties come mainly from two aspects: the strong nonlinearity of governing equations and the irregularity of random porous structures. Coelho et al. [29] developed a direct numerical solution for the EOF in porous media in the linear limit when the EDL thickness was much larger than the elementary grid size, and the method was applied to analyze the electroosmotic phenomena in fractures [50], porous media [51], and compact clays [52,53]. As well known the linear approximation is strictly valid for low zeta potentials, ζ, whose absolute value is smaller than 25 mV [54,55]. Gupta et al. [56] recently extended their linear model to the nonlinear region for high zeta potentials. Since the accuracy of their models depends strongly on the discretization step, their applications are limited by the computational costs [57]. Only a few results with relatively coarse spatial discretization steps have been found to reach reasonable computation times [29,50–54,56]. Kang et al. [58] introduced the interval functions approximation [59] into the Poisson–Boltzmann equation to simplify the solution process and to improve the efficiency. Their method showed good performance in analyzing EOFs in packing microspheres [60,61]. Hlushkou et al. [57] proposed a numerical scheme for modeling the EOF in porous media, involving a traditional finite-difference method (FDM) for solving the Poisson–Nernst–Planck equations for electrodynamics and a lattice Boltzmann method (LBM) for solving the Navier–Stokes equations for hydrodynamics, and investigated the EOFs in spatially regular and random sphere arrays. Recently, Wang et al. [62,63] presented a lattice Poisson–Boltzmann method (LPBM), which combines a lattice Poisson method (LPM) for solving the nonlinear Poisson equation for electric potential distribution [64] with a lattice Boltzmann method for solving the Boltzmann–BGK equations for fluid flow. The LPBM has been employed to analyze the performance improvements by changed porous media additives in micropumps [65] and the morphology effects on EOF in anisotropic porous media [66]. To our knowledge, few contributions have reported a full numerical analysis of EOF in micro- and nanoscale random porous media.

The purpose of this contribution is to present a numerical set and modeling results of three-dimensional EOFs in homogeneously charged micro- and nanoscale random porous media. We extend the random generation-growth method for reproducing microstructures of random porous media, for granular porous media as examples [47,48], and the lattice Poisson–Boltzmann algorithm [62,63,65] into three-dimensional cases. The present numerical set is then employed to analyze the influences of statistical characteristics of solid-media morphology, fluid phase property, and surface potential on the EOF behavior in random porous media. The paper is organized as follows. In Section 2, we present the governing equations along with corresponding boundary conditions. In Section 3, we introduce briefly the employed numerical methods, in particular, the random generation-growth method for generating 3D microstructures of random porous media, and the efficient lattice Poisson–Boltzmann algorithm for solving the governing equations of EOF in porous media. Numerical results are gathered in Section 4, which include a series of simulations addressing the influences of solid, liquid, and interface characteristics on the EOF permeability. Qualitative and quantitative comparisons with existing experimental data are presented in Section 4 and the fluid mechanism is discussed.

2. Governing equations

Although our focus is down to the nanoscale, it is still beyond atomistic effects. Macroscopic continuum assumptions work in their way. Consider an N-component Newtonian electrolyte flowing with velocity $\mathbf{u}(\mathbf{r},t)$ in interstices of a porous material with no polarization and chemical reactions. Let $\psi(\mathbf{r},t)$ be the electric potential prevailing within the solution; the flux $\mathbf{j}_i$ of each ith ion species, composing the solute, is given by the following constitutive equation [67]

$$\mathbf{j}_i = -D_i \nabla n_i - e z_i b_i n_i \nabla\psi + n_i \mathbf{u}, \tag{1}$$

where n_i is the number density of the ith ion species, z_i the ith ion algebraic valence, and e the absolute charge of electron. D_i and b_i are the ion's diffusivity and electric mobility, related by the Stokes–Einstein equation

$$D_i = b_i kT, \tag{2}$$

where k is the Boltzmann constant and T the absolute temperature. The ionic flux $\mathbf{j}_i$ and the concentration n_i obey the continuity equation

$$\frac{\partial n_i}{\partial t} + \nabla\cdot\mathbf{j}_i = 0. \tag{3}$$

For an incompressible laminar electroosmotic flow, the movement of electrolyte is governed by the continuity and momentum equations

$$\nabla\cdot\mathbf{u} = 0, \tag{4}$$

$$\rho\frac{\partial\mathbf{u}}{\partial t} + \rho\mathbf{u}\cdot\nabla\mathbf{u} = \mu\nabla^2\mathbf{u} + \mathbf{F}_E, \tag{5}$$

where ρ is the solution density, μ the dynamic fluid viscosity, and $\mathbf{F}_E$ the electric force density vector. In general, the electrical force in electrokinetic fluids can be expressed as

$$\mathbf{F}_E = \mathbf{F}_{\mathrm{ext}} + \rho_e(\mathbf{E}_{\mathrm{int}} + \boldsymbol{\xi}\times\mathbf{B}_{\mathrm{int}}) + \mathbf{F}_V, \tag{6}$$

where $\mathbf{F}_{\mathrm{ext}}$ represents the external field body forces, including the Lorentz force associated with any externally applied electric and magnetic field. For only an electrical field, $\mathbf{F}_{\mathrm{ext}} = \rho_e\mathbf{E}$, where ρ_e is the net charge density and $\mathbf{E}$ is the electrical field strength. $\mathbf{E}_{\mathrm{int}}$ and $\mathbf{B}_{\mathrm{int}}$ are internally smoothed electrical and magnetic fields due to the motion of the charged particles inside the fluid. $\mathbf{F}_V$ is a single equivalent force density due to the intermolecular attraction [68]. In the present contribution, we are concerned with the steady state of electroosmosis in microporous media so that the electromagnetic susceptibility is negligible. The net charge density ρ_e can be expressed as

$$\rho_e = \sum_i e z_i n_i. \tag{7}$$

The local electrical potential is governed by the Poisson equation

$$\nabla^2\psi = -\frac{\rho_e}{\varepsilon_r\varepsilon_0} = -\frac{1}{\varepsilon_r\varepsilon_0}\sum_{i=1}^{N} e n_i z_i, \tag{8}$$

where ε_r is the dimensionless fluid dielectric constant and ε_0 the permittivity of a vacuum.

Equations (3)–(8) are the governing equations for electroosmosis in porous media and can be solved subject to the following boundary conditions on the liquid–solid interface Ω

$$(\mathbf{v}\cdot\mathbf{j}_i)_\Omega = 0, \tag{9}$$

$$\mathbf{u}_\Omega = 0, \tag{10}$$

$$\psi_\Omega = \zeta, \tag{11}$$

where $\mathbf{v}$ is the outer normal to Ω, and ζ the zeta potential.

For the electroosmotic flow of dilute electrolyte in microporous media, the macroscopic velocity is low so that equilibrium satisfies everywhere in the flow field base on which one can obtain the Boltzmann distribution for n_i

$$n_i = n_{i,\infty}\exp\left(-\frac{e z_i}{kT}\psi\right), \tag{12}$$

where $n_{i,\infty}$ is the bulk ionic number density. Substituting Eq. (12) into Eq. (8) yields the famous nonlinear Poisson–Boltzmann equation for electrokinetic flows [69]:

$$\nabla^2\psi = -\frac{1}{\varepsilon_r\varepsilon_0}\sum_i e z_i n_{i,\infty}\exp\left(-\frac{e z_i}{kT}\psi\right). \tag{13}$$

So far as it is concerned, the present contribution actually solves the governing equations ((4)–(7), (12), and (13)) subject to the boundary conditions Eqs. (9)–(11) by the numerical methods as described in the next section.

3. Numerical methods

This section describes the numerical methods used to simulate EOF in random porous media, including a generation algorithm for three-dimensional random porous microstructures and a mesoscopic PDE solver for the multiphysical transports equations, the lattice Poisson–Boltzmann method.

3.1. Generation of random porous structures

As noted before, the phase distributions are random in a natural porous medium. Although the shapes, positions, and connections of elements are different for different medium samples, one still can measure and summarize essential statistical information of morphology and then reproduce a digital random structure in computers. The generated microstructures may be different from a real one in detail, but they have the same structure characteristics in statistics. Several methods have been proposed to generate random porous structures in the past few years [36–49]. Here we follow the random generation-growth model for reproducing multiphase granular porous microstructures [47,48] and develop the algorithm into three-dimensional cases.

In most cases, the microstructure for EOF flowing through has two phases: solid structure and fluid solution. The process of the multiparameter generation-growth model for such two-phase structures is described below:

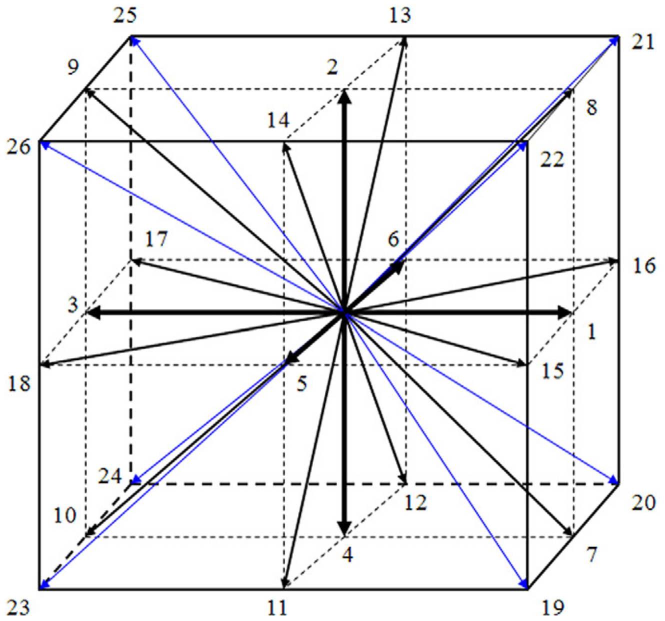

Fig. 1. Twenty-six growth directions of each cell in three-dimensional cubic grid systems.

(i) Randomly locate the cores of solid particles in a grid system based on a core distribution probability, c_d, whose value is no greater than the volume fraction of solid. Each cell in the grid will be assigned a random number by a uniform distribution function within (0, 1). Each cell whose random number is no greater than c_d will be chosen as a core.

(ii) Enlarge every element of the solid particles to its neighboring cells in all directions based on each given directional growth probability, D_i, where i represents the direction. Again for each solid particle, new random numbers will be assigned to its neighboring cells. The neighboring cell in direction i will become part of solid particle if its random number is no greater than D_i.

(iii) Repeat the growing process of (ii) until the volume fraction of the solid particles reaches its given value P_s whose value is usually equal to $(1 - \varepsilon)$ with ε representing the porosity.

Thus the generated microstructure is controlled by the three statistical parameters, c_d, D_i, and P_s (or ε).

The core distribution probability c_d is defined as the probability of a cell to become a core of solid particles. Its value is strongly relative to the number density of solid particles. For a given porosity, the average volume of each solid particle V_p could be related to c_d as $V_p = (1 - \varepsilon)V/(N \cdot c_d)$, where V represents the total volume of the system, and N the total grid number. The value of c_d also controls the degree of structure details for a certain grid system. A smaller c_d leads to a finer description of the microstructures, including particle shapes and interparticle connections. However, a small value of c_d will also decrease the statistical particle number under a certain grid number and thus increase the computation fluctuation.

The directional growth probability D_i is defined as the probability of a cell neighboring in the ith direction to become a part of the solid phase. The directional growth probabilities are classed into three levels based on the directions or on the contact level with the focused cell: main direction (surface contact), side direction (line contact), and diagonal direction (point contact). An appreciable arrangement of the directional growth probabilities may lead to an isotropic structure of porous media. In other words, the growth probabilities can be adjusted to control the degree of anisotropy. For three-dimensional cubic grid systems, each cell has 26 growing directions to its neighbors (see Fig. 1). There are six main directions (1–6), 12 side directions (7–18), and 8 diagonal directions (19–26). To obtain an isotropic structure in such systems, we have to set uniform values within each class of direction, $D_{1\text{–}6}$, $D_{7\text{–}18}$, and $D_{19\text{–}27}$, and the probability ratio is set as $D_{1\text{–}6}{:}D_{7\text{–}18}{:}D_{19\text{–}27} = 8{:}4{:}1$ by assuming the directional growth probability to be consistent with the equilibrium distribution function of density in an isotropic material [70–72].

Fig. 2 shows four schematic illustrations of the generated three-dimensional porous structures using the present random generation-growth method. The stochastic characteristics of phase distribution and connections are depicted quite realistically in the figures. The white parts represent the solid particles and the dark the fluid. The parameters for Fig. 2a are the solid volume fraction $P_s = 0.3$, the solid particle core distribution probability $c_d = 0.01P_s$, and the growth probabilities in six main directions are equal. Fig. 2b shows the structure when the solid volume fraction geminates, where both the volume and the interparticle connections of the solid phase increase. Comparison between Fig. 2a and Fig. 2c shows that a larger value of c_d leads a solid phase that is more dispersive with a smaller averaged particle size. We can also change the media isotropy by varying values of directional growth probabilities in given directions. Fig. 2d shows a generated anisotropic structure where the growth probabilities of the main directions 1 and 3 enlarge to 10 times. Directional characteristics appear in the structure of Fig. 2d when compared with that in Fig. 2a.

3.2. Lattice Poisson–Boltzmann method

After porous structures are generated, the set of coupled hydrodynamic and electrodynamic governing equations for the EOF subjected to the appropriate boundary conditions will be solved by the lattice Poisson–Boltzmann method which combines an electrical potential evolution on discrete lattices to solve the nonlinear Poisson equation (lattice Poisson method) with a density evolution method on the same set of discrete lattices to solve the Boltzmann–BGK equation (lattice Boltzmann method). Details of two-dimensional LPBM can be found in our previous publications [62,65]. In this work, we develop the LPBM into its three-dimensional form. The equations are only solved in the liquid phase and the solid phase is silent and charged homogeneously on the surfaces.

The continuity and momentum equations can be solved by tracking the movements of molecule ensembles through the evolution of the distribution function using the popular lattice Boltzmann method [73]. The lattice Boltzmann equation can be derived from the Boltzmann equation [74]. For the flows with external forces, the continuous Boltzmann–BGK equation with

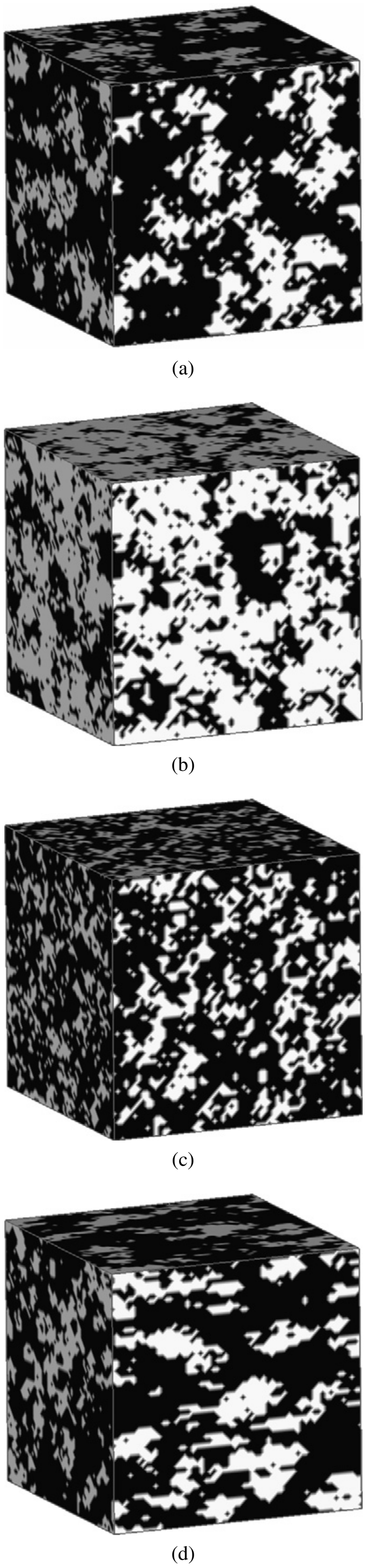
(a)

(b)

(c)

(d)

Fig. 2. Schematics of the generated porous structures using the present growth-generation method on 60 × 60 × 60 grid systems. The white is solid particles and the dark is fluid. (a) $P_s = 0.3$, $c_d = 0.01P_s$; (b) $P_s = 0.6$, $c_d = 0.01P_s$; (c) $P_s = 0.3$, $c_d = 0.1P_s$; (d) $P_s = 0.3$, $c_d = 0.01P_s$, $D_{1,3} = 10D_{2,4\text{–}6}$ (anisotropic).

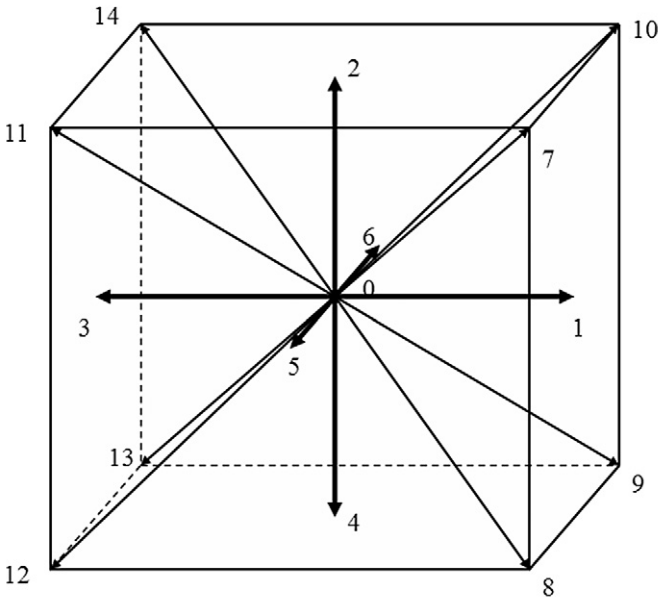

Fig. 3. The lattice direction system (α) for the D3Q15 model.

an external force term, F, is

$$\frac{Df}{Dt} \equiv \partial_t f + (\boldsymbol{\xi} \cdot \nabla) f = -\frac{f - f^{\mathrm{eq}}}{\tau_\nu} + F, \tag{14}$$

where $f \equiv f(x, \boldsymbol{\xi}, t)$ is the single particle distribution function in the phase space $(x, \boldsymbol{\xi})$, $\boldsymbol{\xi}$ the microscopic velocity, τ_ν the relaxation time, f^{eq} the Maxwell–Boltzmann equilibrium distribution, and F the external force term

$$F = \frac{\mathbf{G} \cdot (\boldsymbol{\xi} - \mathbf{u})}{RT} f^{\mathrm{eq}}, \tag{15}$$

with $\mathbf{G}$ being the external force per unit mass [75]. The Chapman–Enskog expansion can be used to transform the Boltzmann–BGK equation, Eq. (7), into the correct continuum Navier–Stokes equations [76].

Thus the three-dimensional 15-speed (D3Q15) discrete density evolution equation is

$$\begin{aligned} &f_\alpha(\mathbf{r} + \mathbf{e}_\alpha \delta_t, t + \delta_t) - f_\alpha(\mathbf{r}, t) \\ &\quad = -\frac{1}{\tau_\nu}\left[f_\alpha(\mathbf{r}, t) - f_\alpha^{\mathrm{eq}}(\mathbf{r}, t)\right] + \delta_t F_\alpha, \end{aligned} \tag{16}$$

where $\mathbf{r}$ is the position vector, δ_t the time step, $\mathbf{e}_\alpha$ the discrete velocities with the direction system shown in Fig. 3,

$$\mathbf{e}_\alpha = \begin{cases} (0, 0, 0), & \alpha = 0, \\ (\pm 1, 0, 0)c,\ (0, \pm 1, 0)c,\ (0, 0, \pm 1)c, & \alpha = 1\text{–}6, \\ (\pm 1, \pm 1, \pm 1)c, & \alpha = 7\text{–}14, \end{cases} \tag{17}$$

where c represents the sound speed, τ_ν the dimensionless relaxation time which is a function of the fluid viscosity,

$$\tau_\nu = 3\nu \frac{\delta_t}{\delta_x^2} + 0.5, \tag{18}$$

where ν is the kinetic viscosity and δ_x the lattice constant (or grid size), and f_α^{eq} the density equilibrium distribution

$$f_\alpha^{\mathrm{eq}} = \omega_\alpha \rho \left[1 + 3\frac{\mathbf{e}_\alpha \cdot \mathbf{u}}{c^2} + 9\frac{(\mathbf{e}_\alpha \cdot \mathbf{u})^2}{c^4} - \frac{3\mathbf{u}^2}{2c^2}\right] \tag{19}$$

with

$$\omega_\alpha = \begin{cases} 2/9, & \alpha = 0, \\ 1/9, & \alpha = 1\text{–}6, \\ 1/72, & \alpha = 7\text{–}14. \end{cases} \tag{20}$$

For EOFs of dilute electrolyte solutions, the external electrical force in Eq. (2) can be simplified to

$$\mathbf{F}_E = \rho_e \mathbf{E} - \rho_e \nabla \Phi, \tag{21}$$

where Φ is the stream electrical potential caused by the ion movements in the solution based on the Nernst–Planck theory. Generally, the stream potential dominates the electro-viscosity effect in pressure driven flows, but its value is much less than the external potential and can be ignored in electrically driven flows. Therefore, the external force in the discrete lattice Boltzmann equation is

$$F_\alpha = \frac{\rho_e \mathbf{E} \cdot (\mathbf{e}_\alpha - \mathbf{u})}{\rho R T} f_\alpha^{\text{eq}}. \tag{22}$$

The macroscopic density and velocity can be calculated using

$$\rho = \sum_\alpha f_\alpha, \tag{23}$$

$$\rho \mathbf{u} = \sum_\alpha \mathbf{e}_\alpha f_\alpha. \tag{24}$$

To solve the Poisson equation with strong nonlinearity, Eq. (13), we employ here another evolution method on the same grid system, lattice Poisson method [64], by tracking the electrical potential distribution transporting on the discrete lattices. By expanding Eq. (13) into the time-dependent form

$$\frac{\partial \psi}{\partial t} = \nabla^2 \psi + g_{\text{rhs}}(\mathbf{r}, \psi, t), \tag{25}$$

with $g_{\text{rhs}} = \frac{1}{\varepsilon \varepsilon_0} \sum_i z_i e n_{i,\infty} \exp(-\frac{z_i e}{k_b T} \psi)$ representing the *negative* right-hand side (RHS) term of the original Eq. (13), we get the discrete evolution equation for the electrical potential distribution

$$\begin{aligned} &g_\alpha(\mathbf{r} + \Delta \mathbf{r}, t + \delta_{t,g}) - g_\alpha(\mathbf{r}, t) \\ &\quad = -\frac{1}{\tau_g}\left[g_\alpha(\mathbf{r}, t) - g_\alpha^{\text{eq}}(\mathbf{r}, t)\right] + \left(1 - \frac{0.5}{\tau_g}\right)\delta_{t,g}\omega_\alpha g_{\text{rhs}}, \end{aligned} \tag{26}$$

where the equilibrium distribution of the electric potential evolution variable g is

$$g_\alpha^{\text{eq}} = \varpi_\alpha \psi \qquad \text{with } \varpi_\alpha = \begin{cases} 0, & \alpha = 0, \\ 1/9, & \alpha = 1\text{–}6, \\ 1/72, & \alpha = 7\text{–}14. \end{cases} \tag{27}$$

The time step for the electrical potential evolution is

$$\delta_{t,g} = \frac{\delta_x}{c'}, \tag{28}$$

where c' is a *pseudo* sound speed in the potential field [62]. The dimensionless relaxation time is

$$\tau_g = \frac{3\chi \delta_{t,g}}{2\delta_x^2} + 0.5, \tag{29}$$

where χ is defined as the potential diffusivity which equals to unity in these simulations.

After evolving on the discrete lattices, the macroscopic electrical potential can be calculated using

$$\psi = \sum_\alpha (g_\alpha + 0.5\delta_{t,g} g_{\text{rhs}} \omega_\alpha). \tag{30}$$

Though the electrical potential evolution equations are in an unsteady form, only the steady-state result is realistic, because the electromagnetic susceptibility has not been considered. Although the lattice evolution method for the nonlinear Poisson equation is not as efficient as the multigrid solutions due to its long wavelength limit, it has the advantages of suitability for geometrical complexity and parallel computing [64].

The boundary condition implements play a very critical role in the accuracy of the numerical simulations. The hydrodynamic boundary conditions for the lattice Boltzmann method have been studied extensively [77–84]. The conventional bounce-back rule is the most commonly used method to treat the velocity boundary condition at the solid–fluid interface due to its easy implementation, where momentum from an incoming fluid particle is bounced back in the opposite direction as it hits the wall [76]. However the conventional bounce-back rule has two main disadvantages. First, it requires the dimensionless relaxation time strictly within the range of (0.5, 2), otherwise the prediction will deviate from the correct result definitely [77,78]. Second, the nonslip boundary implemented by the conventional bounce-back rule is not located on the boundary nodes exactly, which will lead to inconsistencies when coupling with other PDE solvers on a same grid set [79].

To overcome the inconsistency between the LBM and the other PDE solvers on a same grid set, one can replace the bounce-back rule with another “nonslip” boundary treatment proposed by Inamuro et al. [80], with the cost of loss of easy implementation for complicated geometries. An alternative solution is to modify the boundary condition treatments of the PDE solver for the electric potential distribution to be consistent with the LBM bounded by the bounce-back rule. In this contribution, the bounce-back rule [79,81] for nonequilibrium distribution proposed by Zou and He [82] is introduced and extended to both hydrodynamic and electrodynamic boundary implementations to deal with the complex geometries in porous media.

At the boundary the following hydrodynamic boundary condition holds,

$$f_\alpha^{\text{neq}} = f_\beta^{\text{neq}}, \tag{31}$$

where the subscripts α and β represent opposite directions.

Analogously, the nonequilibrium “bounce-back” rule for the electric potential distribution at the wall surfaces is suggested as

$$g_\alpha^{\text{neq}} = -g_\beta^{\text{neq}}. \tag{32}$$

These boundary treatments are easy to implement for complicated geometries and have approximately second-order accuracy [79,82].

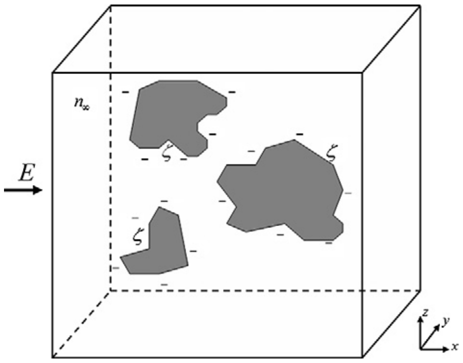

Fig. 4. Schematic illustration of EOF in charged random porous media.

4. Results and discussion

Fig. 4 shows a schematic illustration of three-dimensional EOF in charged random porous media. The solid microstructure has random shapes, positions, and connections, generated by the algorithm described in Section 3.1. The cubic domain is periodic in all three directions. The solid surfaces are homogeneously charged with a zeta potential, ζ, so that the electrolyte solution can be driven flowing though the porous structure by an external electrical field, **E**. In this section, we simulate and analyze EOFs in charged microporous media using the lattice Poisson–Boltzmann method, with geometry, solution, and surface charge effects considered. The simulated results are compared with existing theories and experimental data.

In the following simulations, we focus on a cubic system each side of which is 1 μm long. A $60 \times 60 \times 60$ uniform grid is used. We change microstructure geometries of porous media by varying the porosity ε from 0.1 to 0.9. The average characteristic length of particles varies from 20 to 150 nm. The bulk ionic concentration n_∞ varies from 10^{-6} to 10^{-3} M and the surface zeta potential from 0 to -100 mV. The other properties and parameters used in this work are as follows: the fluid density $\rho = 999.9\ \mathrm{kg/m^3}$, the dielectric constant $\varepsilon_r \varepsilon_0 = 6.95 \times 10^{-10}\ \mathrm{C^2/J\,m}$, the dynamic viscosity $\mu = 0.889$ mPa s, the temperature $T = 273$ K, and the external electrical field strength $E = 1 \times 10^4$ V/m.

4.1. Geometry effects

First, the geometry effects on the electroosmotic permeability in microporous media are investigated by changing the volume fraction and particle size (or number density) of the solid phase. We define the electroosmotic permeability, κ_e, as

$$\kappa_e = \frac{\bar{u}}{E}, \tag{33}$$

where $\bar{u}$ is the averaged velocity of EOF along the direction of the driving electrical field **E**.

The coefficients of electroosmotic permeability (κ_e) for different porosities (ε) of porous media are shown in Fig. 5. The other parameters are $c_d = 0.1$ for the microstructure generation process, the bulk molar concentration $c_\infty = 10^{-4}$ M, and $\zeta = -50$ mV. The electroosmotic permeability increases with the porosity monotonically. The increasing rate rises with the porosity as well which is very low when the porosity is smaller than 0.5 and becomes sharply high when the porosity is larger than 0.7. The predicted electroosmotic permeability is in the order of $10^{-9}\ \mathrm{m^2/s\,V}$, which is consistent with the existing experimental measurements [83].

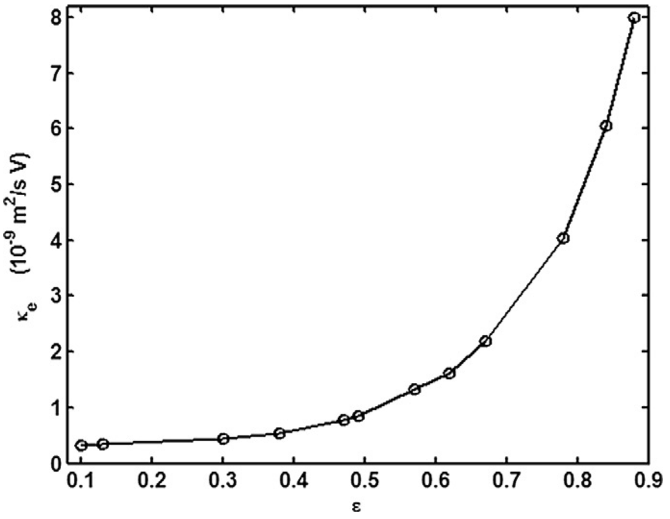

Fig. 5. Predicted electroosmotic permeabilities for various porosities of porous media at $c_\infty = 10^{-4}$ M, $\zeta = -50$ mV, $E = 1 \times 10^4$ V/m.

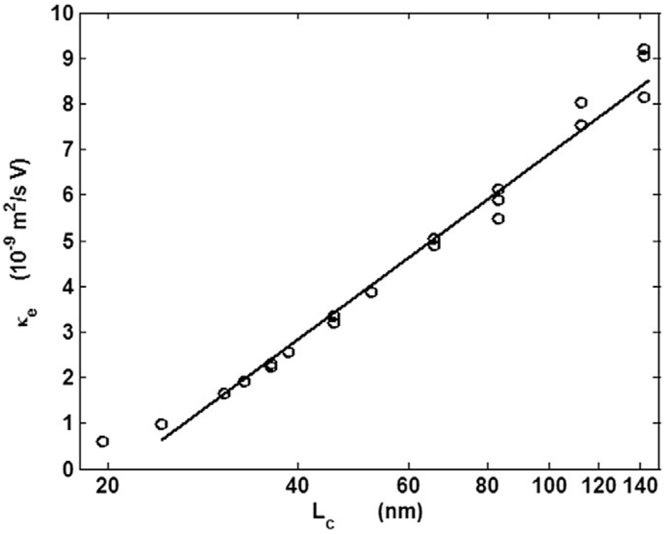

Fig. 6. The electroosmotic permeability versus average characteristic length of solid particles for $\varepsilon = 0.38$, $c_\infty = 10^{-4}$ M, $\zeta = -50$ mV, and $E = 1 \times 10^4$ V/m.

Fig. 6 shows the calculated electroosmotic permeability in homogeneously charged nanoscale porous media versus the average characteristic length of solid particles which is defined as the cube root of the average volume of every particle. The average characteristic length changes from 20 to 150 nm by varying c_d from 0.38 to 0.001 in the present simulations and other parameters are $\varepsilon = 0.38$, $c_\infty = 10^{-4}$ M, and $\zeta = -50$ mV. The results show that the electroosmotic permeability κ_e increases with the average characteristic length of solid particles monotonically. When the x-axial is in a logarithmic scale, the

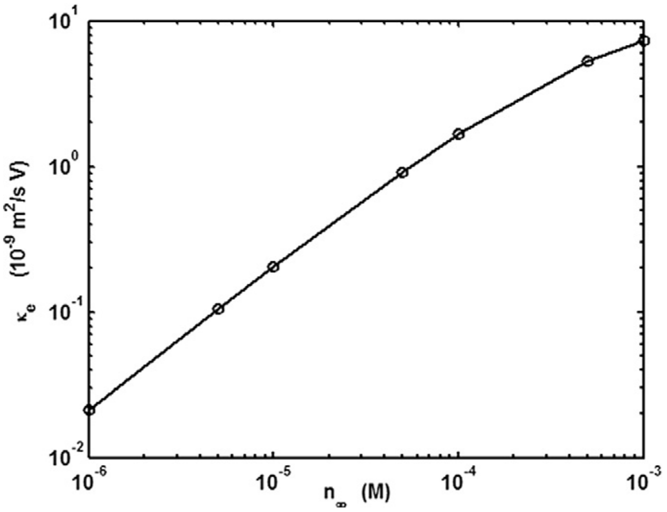

Fig. 7. The electroosmotic permeability changing with the bulk ionic concentration for $\varepsilon = 0.38$, $\zeta = -50$ mV, and $E = 1 \times 10^4$ V/m.

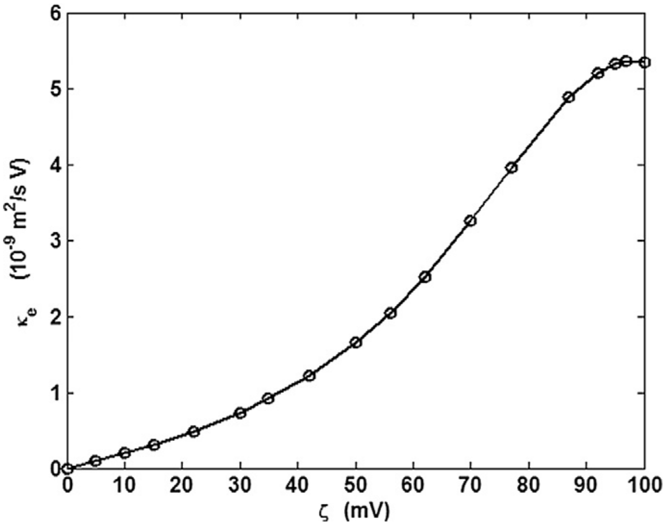

Fig. 8. The electroosmotic permeability versus the zeta potential for $\varepsilon = 0.38$, $c_\infty = 10^{-4}$ M, and $E = 1 \times 10^4$ V/m.

curve appears nearly linear (see the reference line in Fig. 6), which means that the electroosmotic permeability increases with the average characteristic length of particles at an approximately logarithmic rate. Three trials were performed for each average characteristic length but the calculated electroosmotic permeabilities did not exactly fall into a same value. The fluctuations come from the stochastic characteristics of the random microstructure. For a given porosity and a grid number, a smaller average characteristic length of particles leads to a smaller statistical fluctuation around the average result. For parameters used in the present contribution, the statistical deviation is smaller than 3%.

4.2. Concentration effect

Based on the macroscopic EOF theory, the electrical double layer can often be treated as a thin layer and a slip velocity can therefore be introduced by the Helmholtz–Smoluchowski model,

$$\mathbf{u}_{\text{slip}} = -\frac{\varepsilon_0 \varepsilon_r \zeta \mathbf{E}}{\mu}, \tag{34}$$

as a boundary condition subject to the hydrodynamic equations (Eqs. (4) and (5)). Such models have been employed to analyze the EOF in microporous media frequently [19–22,25–35]. A further conclusion from Eq. (34) is that the electroosmotic permeability has no relationship with the ionic concentration of the electrolyte solution. This may be true if the solid individuals are separated by a wide enough interval space. However, in most natural microporous media, such a critical condition is hard to satisfy. The narrow clearances between solid particles of microporous media often break down the thin double-layer approximation and the EOF should be governed by the full set of equations (Eqs. (4)–(13)).

Fig. 7 shows the predicted electroosmotic permeability versus the bulk ionic concentration of the electrolyte solution. We used a same porous microstructure with $c_d = 0.1$ and $\varepsilon = 0.38$. The electroosmotic permeability κ_e increase monotonically with the bulk ionic concentration c_∞ as c_∞ varies from 10^{-6} to 10^{-3} M. This result can be explained by the undeveloped electrical potential distributions in narrow channels, whose similar results can be found in Fig. 2 of Ref. [66] and Figs. 1 and 2 of Ref. [84]. When c_∞ is lower than 10^{-4} M, the electroosmotic permeability is nearly proportional to the bulk ionic concentration. When c_∞ is higher, the increasing rate becomes a little smaller.

4.3. Zeta potential effects

Zeta potential on solid surfaces of porous media affects EOF permeability directly. Simple proportional relationships have been obtained between the electroosmotic permeability and the zeta potential for electrical transports in soils [83,85] and in polymer composites recently based on the boundary-layer theory [86]. Here we analyze such effects using our numerical methods.

Fig. 8 shows the calculated electroosmotic permeability versus the zeta potential on solid surfaces of porous media. All surfaces are homogeneously charged with a same value of ζ. The other parameters used are $c_\infty = 10^{-4}$ M, $c_d = 0.1$, and $\varepsilon = 0.38$. The zeta potential ζ changes from 0 to 100 mV. It shows that the proportionally linear relationship between electroosmotic permeability and zeta potential is accurate only when ζ is very small (<30 mV). The permeability increases much sharper when the zeta potential ζ is larger than 40 mV and then smoother when the zeta potential ζ is larger than 90 mV.

4.4. Comparison with experiments

The predicted electroosmotic permeability is also compared with experimental data quantitatively for different zeta potentials. Table 1 listed six kinds of soil and the measured data, including porosities, zeta potentials, and permeabilities [87]. Since there is little information about the soil structure and

Table 1
Electroosmotic permeability for different soils

Soil	ε	ζ (mV)	κ_e, measured (10^{-9} m^2/s V)	κ_e, H-S model (10^{-9} m^2/s V)	κ_e, predicted (10^{-9} m^2/s V)
Gray	0.53	64	0.72	45	0.74[a]
Brown	0.62	97	2.86	69	2.0[b]
G–H	0.62	96	2.00	68	2.0[b]
Phosphatic	0.87	62	0.7	44	1.72[c]
Wallace burg	0.51	87	1.5	62	1.6[a]
Orleans	0.70	22	0	16	0.052[c]

The parameters used for predictions are:
[a] $c_d = 0.1 P_s$ and $n_e = 2 \times 10^{-5}$ M.
[b] $c_d = P_s$ and $n_e = 1 \times 10^{-5}$ M.
[c] $c_d = P_s$ and $n_e = 1 \times 10^{-4}$ M.

the properties of electrolyte solutions, we evaluate such values by referring to some relative references [87–89]. Table 1 also compares the predictions based on the H–S model [83,87] which are one order of magnitude higher than the experimental data. It is shown that the predicted electroosmotic permeabilities by the present method agree much better with the measured data.

5. Conclusions

Electroosmosis in homogeneously charged micro- and nanoscale random porous media has been numerically investigated using the mesoscopic simulation methods. A random generation-growth method has been developed for reproducing three-dimensional random microstructures of natural porous media and the high-efficiency lattice Poisson–Boltzmann algorithm has been extended into three-dimensional cases for solving the strongly nonlinear governing equations of electroosmosis in random porous media. Such a full numerical set is quite suitable for analyses of electroosmosis in micro- and nanoscale random porous media.

The numerical modeling and predictions of EOF in microporous media indicate that the electroosmotic permeability increases monotonically with the porosity of random porous media and the increasing rate rises with the porosity as well; the electroosmotic permeability increases with average solid particle size for certain porosity; the permeability increases with the bulk ionic concentration in microporous media which cannot be predicted based on the macroscopic theory; the proportional relationship between the electroosmotic permeability and the zeta potential stands only at low zeta potentials. The present predictions agree with the existing experimental observations and measurements. The results and methodology in this contribution may be of great significance for improving our understandings of multiphysical transport mechanisms in electroosmosis in micro- and nanoscale random porous media.

Acknowledgments

The present work is supported by a Grant from the NTC-M04-CD01 and NSF-061308.

References

[1] A.E. Alexander, P. Jonson, Colloid Science, Clarendon, Oxford, 1949.
[2] A.P. Shapiro, P.C. Renaud, R.F. Probstein, Physicochem. Hydrodyn. 11 (1989) 785–802.
[3] A. Ugaz, S. Puppala, R.J. Gale, Y.B. Acar, Chem. Eng. Commun. 129 (1994) 183–200.
[4] K.P. Tikhomolova, Electro-Osmosis, Ellis Horwood, New York, 1993.
[5] A.L. Crego, A. Gonzalez, M.L. Marina, Crit. Rev. Anal. Chem. 26 (4) (1996) 261–304.
[6] T. Paillat, E. Moreau, P.O. Grimaud, G. Touchard, IEEE Trans. Dielect. Elect. Insul. 7 (5) (2000) 693–704.
[7] F. Reuss, Mem. Soc. Imp. Nat. Moscou 2 (1809) 327–337.
[8] A.K. Banga, Electrically Assisted Transdermal and Topical Drug Delivery, Taylor & Francis, London, 1998.
[9] R.E. Oosterbroek, A. van den Berg, Lab-on-a-Chip: Miniaturized Systems for (Bio)Chemical Analysis and Síntesis, Boston, Elsevier, 2003.
[10] P.K. Wong, J.T. Wang, J.H. Deval, C.M. Ho, IEEE/ASME Trans. Mech. 9 (2004) 366–376.
[11] J.H. Masliyah, S. Bhattacharjee, Electrokinetic and Colloid Transport Phenomena, Wiley, New York, 2006.
[12] D. Beamish, R.J. Peart, Terra Nova 10 (1) (1998) 48–55.
[13] C.Y. Wang, Chem. Rev. 104 (2004) 4727–4766.
[14] L. Ma, D.B. Ingham, M.C. Pourkashanian, in: D.B. Ingham, I. Pop (Eds.), Transport Phenomena in Porous Media III, Elsevier, San Diego, 2005, pp. 418–440.
[15] S.D. Harris, Q.J. Fisher, M. Karimi-Fard, A.Z. Vaszi, K. Wu, in: D.B. Ingham, I. Pop (Eds.), Transport Phenomena in Porous Media III, Elsevier, San Diego, 2005, pp. 441–476.
[16] H.A. Stone, A.D. Stroock, A. Ajdari, Annu. Rev. Fluid Mech. 36 (2004) 381–411.
[17] D.Q. Li, Electrokinetics in Microfluidics, Academic, Oxford, 2004.
[18] G.E. Karniadakis, A. Beskok, N.R. Aluru, Microflows and Nanoflows: Fundamentals and Simulation, Springer-Verlag, New York, 2005.
[19] P.H. Paul, D.W. Arnold, D.J. Rakestraw, MicroTAS '98, Kluwer Academic, Dordrecht, 1998.
[20] S.L. Zeng, C.H. Chen, J.C. Mikkelsen, J.G. Santiago, Sens. Actuators B 79 (2–3) (2001) 107–114.
[21] S.H. Yao, J.G. Santiago, J. Colloid Interface Sci. 268 (1) (2003) 133–142.
[22] J.A. Tripp, F. Svec, J.M.J. Frechet, S.L. Zeng, J.C. Mikkelsen, J.G. Santiago, Sens. Actuators B 99 (1) (2004) 66–73.
[23] Y.J. Kang, S.C. Tan, C. Yang, X.Y. Huang, Sens. Actuators A 133 (2) (2007) 375–382.
[24] F.C. Leinweber, J.C.T. Eijkel, J.G. Bomer, A. van den Berg, Anal. Chem. 78 (2006) 1425–1434.
[25] S. Levine, G.H. Neale, J. Colloid Interface Sci. 47 (2) (1974) 520–528.
[26] R.F. Probstein, Physicochemical Hydrodynamics: An Introduction, Wiley, New York, 1994.
[27] S. Marino, D. Coelho, S. Bekri, P.M. Adler, J. Colloid Interface Sci. 223 (2) (2000) 292–304.
[28] E.K. Zholkovskij, S.S. Dukhin, N.A. Mishchuk, J.H. Masliyah, J. Czarnecki, Colloids Surf. A 192 (1–3) (2001) 235–251.
[29] D. Coelho, M. Shapiro, J.F. Thovert, P.M. Alder, J. Colloid Interface Sci. 181 (1) (1996) 169–190.
[30] L. Dresner, J. Phys. Chem. 67 (8) (1963) 1635.
[31] G.D. Mehta, T.F. Morse, J. Chem. Phys. 63 (5) (1975) 1878–1889.
[32] M.Q. Jin, M.M. Sharma, J. Colloid Interface Sci. 142 (1) (1991) 61–73.
[33] B.A. Grimes, J.J. Meyers, A.I. Liapis, J. Chromatogr. A 890 (2000) 61–72.
[34] M.W. Kozak, E.J. Davis, J. Colloid Interface Sci. 112 (2) (1986) 403–411.
[35] H. Ohshima, J. Colloid Interface Sci. 210 (1999) 397–399.
[36] L. Tacher, P. Perrochet, A. Parriaux, Transport Porous. Med. 26 (1) (1997) 99–107.
[37] M. Pilotti, Transport Porous. Med. 33 (3) (1998) 257–278.
[38] K. Makrodimitris, G.K. Papadopoulos, C. Philippopoulos, D.N. Theodorou, J. Chem. Phys. 117 (2002) 5876–5884.
[39] D.S. Li, G. Saheli, M. Khaleel, H. Garmestani, Comput. Mater. Sci. 38 (1) (2006) 45–50.
[40] N. Losic, J.F. Thovert, P.M. Adler, J. Colloid Interface Sci. 186 (1997) 420–433.

[41] S. Torquato, Random Heterogeneous Materials: Microstructure and Macroscopic Properties, Springer-Verlag, New York, 2002.

[42] S. Torquato, Int. J. Solids Struct. 37 (2000) 411–422.

[43] I.M. Young, J.W. Crawford, C. Rappoldt, Soil Till. Res. 61 (2001) 33–45.

[44] K.J. Wu, N. Nunan, J.W. Crawford, I.M. Young, K. Ritz, Soil Sci. Soc. Am. J. 68 (2004) 346–351.

[45] P. Meakin, Fractals, Scaling and Growth Far from Equilibrium, Cambridge Univ. Press, Cambridge UK, 1998.

[46] P.V. Coveney, J.B. Maillet, J.L. Wilson, P.W. Fowler, O. Al-Mushadani, B.M. Boghosian, Int. J. Mod. Phys. C 9 (8) (1998) 1479–1490.

[47] M. Wang, J.K. Wang, N. Pan, S.Y. Chen, Phys. Rev. E 75 (2007) 036702.

[48] M. Wang, J.K. Wang, N. Pan, S.Y. Chen, J.H. He, J. Phys. D 40 (2007) 260–265.

[49] M. Wang, J.H. He, J.Y. Yu, N. Pan, Int. J. Thermal Sci. (2007), doi:10.1016/j.ijthermalsci.2006.11.006.

[50] S. Marino, D. Coelho, S. Bekri, P.M. Adler, J. Colloid Interface Sci. 223 (2) (2000) 292–304.

[51] S. Marino, M. Shapiro, P.M. Adler, J. Colloid Interface Sci. 243 (2) (2001) 391–419.

[52] M. Rosanne, M. Paszkuta, J.F. Thovert, P.M. Adler, Geophys. Res. Lett. 31 (18) (2004) L18614.

[53] M. Rosanne, M. Paszkuta, P.M. Adler, J. Colloid Interface Sci. 297 (1) (2006) 353–364.

[54] S. Levine, J.R. Marriott, G. Neale, N. Epstein, J. Colloid Interface Sci. 52 (1) (1975) 136–149.

[55] R.J. Flatt, P. Bowen, Cem. Concr. Res. 33 (6) (2003) 781–791.

[56] A.K. Gupta, D. Coelho, P.M. Adler, J. Colloid Interface Sci. 303 (2006) 593–603.

[57] D. Hlushkou, A. Seidel-Morgenstern, U. Tallarek, Langmuir 21 (13) (2005) 6097–6112.

[58] Y.J. Kang, C. Yang, X.Y. Huang, J. Colloid Interface Sci. 253 (2) (2002) 285–294.

[59] J.R. Philip, R.A. Wooding, J. Chem. Phys. 52 (2) (1970) 953.

[60] Y.J. Kang, C. Yang, X.Y. Huang, Int. J. Eng. Sci. 42 (19–20) (2004) 2011–2027.

[61] Y.J. Kang, C. Yang, X.Y. Huang, Microfluidics Nanofluidics 1 (2) (2005) 168–176.

[62] J.K. Wang, M. Wang, Z.X. Li, J. Colloid Interface Sci. 296 (2) (2006) 729–736.

[63] M. Wang, J.K. Wang, Z.X. Li, J. Colloid Interface Sci. 300 (1) (2006) 446.

[64] Wang J.K., Wang M., Li Z.X., Commun. Nonlinear Sci. Numer. Simul. (2006), doi:10.1016/j.cnsns.2006.06.002, in press.

[65] M. Wang, J.K. Wang, S.Y. Chen, N. Pan, J. Colloid Interface Sci. 304 (1) (2006) 246–253.

[66] M. Wang, J.K. Wang, N. Pan, S.Y. Chen, Commun. Comput. Phys. (2007), in press.

[67] V.G. Levich, Physico-Chemical Hydrodynamics, Prentice–Hall, New York, 1962.

[68] B.M. Li, D.Y. Kwok, J. Colloid Interface Sci. 263 (1) (2003) 144–151.

[69] B. Honig, A. Nicholls, Science 268 (5214) (1995) 1144–1149.

[70] X. He, L.S. Luo, Phys. Rev. E 55 (1997) 6333–6336.

[71] T. Abe, J. Comput. Phys. 131 (1997) 241–246.

[72] Y. Peng, C. Shu, Y.T. Chew, J. Comput. Phys. 193 (2003) 260–274.

[73] S.Y. Chen, G.D. Doolen, Annu. Rev. Fluid Mech. 30 (1998) 329–364.

[74] X.Y. He, L.S. Luo, Phys. Rev. E 56 (6) (1997) 6811–6817.

[75] X.Y. He, S.Y. Chen, G.D. Doolen, J. Comput. Phys. 42 (146) (1998) 282–300.

[76] Y.H. Qian, D. Dhumieres, P. Lallemand, Europhys. Lett. 17 (1992) 479–484.

[77] D.R. Noble, S.Y. Chen, J.G. Georgiadis, R.O. Buckius, Phys. Fluids 7 (1995) 203–209.

[78] S.Y. Chen, D. Martinez, R.W. Ren, Phys. Fluids 8 (1996) 2527–2536.

[79] M. Rohde, D. Kandhai, J.J. Derksen, H.E.A. van den Akker, Phys. Rev. E 67 (6) (2003) 066703.

[80] T. Inamuro, M. Yoshino, F. Ogino, Phys. Fluids 7 (12) (1995) 2928–2930.

[81] D.P. Ziegler, J. Stat. Phys. 71 (5/6) (1993) 1171–1177.

[82] Q.S. Zou, X.Y. He, Phys. Fluids 9 (6) (1997) 1591–1598.

[83] J.K. Mitchell, K. Soga, Fundamentals of Soil Behavior, third ed., Wiley, New York, 2005.

[84] M. Wang, J.K. Wang, S.Y. Chen, J. Comput. Phys. (2007) doi:10.1016/j.jcp.2007.05.001.

[85] J.Q. Shang, K.Y. Lo, R.M. Quigley, Can. Geotech. J. 31 (5) (1994) 624–636.

[86] R.J. Hill, J. Fluid Mech. 551 (2006) 405–433.

[87] J.Q. Shang, Can. Geotech. J. 34 (1997) 627–631.

[88] J.Q. Shang, K.Y. Lo, J. Hazard. Mater. 55 (1–3) (1997) 117–133.

[89] D.C. Edmeades, D.M. Wheeler, O.E. Clinton, Aust. J. Soil Res. 23 (2) (1985) 151–165.